ORIGINAL ARTICLE

Dynamic modeling and stability prediction in robotic machining

Said Mousavi[1,2] · Vincent Gagnol[1,2] · Belhassen C. Bouzgarrou[1,2] · Pascal Ray[3]

Abstract Machining with anthropomorphic robotic manipulators is used to increase the flexibility and reduce the costs of production. Productivity in robotic machining processes is limited by low rigidity of robot structure and vibration instability in machining (chatter). Vibration instability analysis in robotic machining process is a challenging issue due to the variability of the dynamic behavior of the robot within its workspace. Hence, a dynamic model which correctly takes these variations into account is important to define the cutting parameters and the robot configurations to be adapted along a machining trajectory. In this paper, a multi-body dynamic model of a serial robot is elaborated using beam elements which can easily be integrated into the machining trajectory planning. The beam element geometry, elasticity, and damping parameters are adjusted on the basis of experimental identifications. A stability diagram based on regenerative chatter in milling operations as a function of the kinematic redundancy variable is established. It is shown that stability in robotic machining can be ensured through the optimization of the robot configurations, without changing the cutting parameters, in order to maintain productivity performance. The predicted stability diagram is validated by experimental robotic machining results.
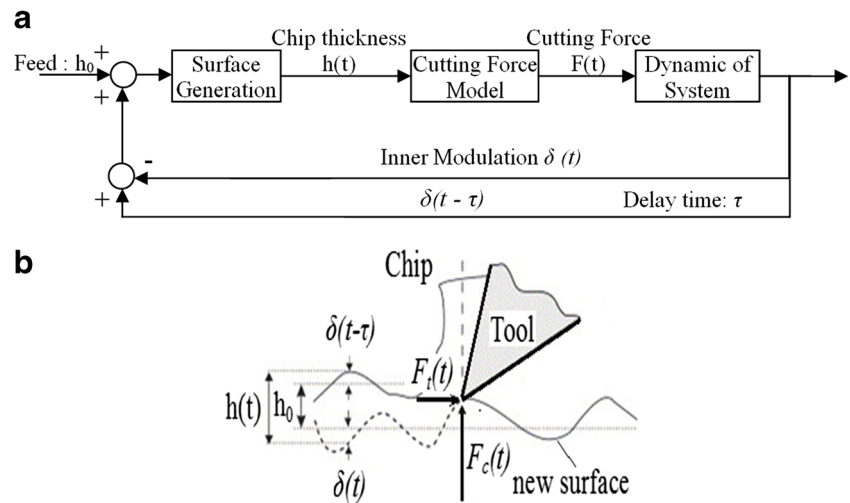
✉ Said Mousavi
said.mousavi@ifma.fr

1 SIGMA Clermont, Institut Pascal, Université Clermont Auvergne, BP 10448, 63000 Clermont Ferrand, France

2 CNRS, UMR 6602, IP, 63178 Aubière, France

3 Mines Saint-Etienne, 158, cours Fauriel, CS 62362, 42023 Saint-Etienne Cedex 2, France

1 Introduction

Technical advances in anthropomorphic robots position them as serious competitors to conventional machine tools in terms of precision, load capacity, and flexibility. Industrial robots are mainly used for pre-machining and the machining or other post-casting applications in the foundry industry with a high-productivity requirement. In order to increase the removal rate, which gives a shorter machining cycle time and high productivity, cutting volume and cutting speed should be increased. These parameters are limited by the low rigidity of the robot structure and the appearance of chatter vibrations. This paper addresses the machining chatter vibrations in the robotic machining process.

Tobias et al. [1] and Altintas [2] present the regeneration of waviness (Fig. 1b) as the most powerful source of chatter and self-excited vibration. The regenerative chatter vibration system can be represented by the block diagram as shown in Fig. 1a.

The dynamic behavior of a robot within the workspace depends on its configuration. Each posture has its own dynamic behavior and stability conditions [4]. Thus, a dynamic model of a robot, which correctly takes these variations into account, is essential in order to analyze the stability of machining operation and optimize the cutting parameters. In this way, several researchers have devoted their studies to the dynamic modeling and identification of the dynamic behavior in order to optimize the precision in robotic machining with respect to their poses.

Mejri et al. [5] experimentally investigated the end-effector position effect on the dynamic behavior of an ABB IRB6660 robot. They observed modifications in the robot's dynamic

Fig. 1 **a** Block diagram of regenerative chatter vibrations; **b** chip thickness variation in regenerative chatter [3]

behavior depending on changes in its posture. The experimental identification enables the determination of the actual dynamic parameters of the robot structure, but they are valid for a given position and configuration where the tests are performed. It cannot predict the robot dynamic behavior along a trajectory. Moreover, experimental identifications are very expensive and time-consuming, but they are usually required as an effective means to calibrate numerical models [6].

Two approaches are generally used for numerical modeling of the robot's dynamic behavior: (a) flexible joints and rigid bodies approach and (b) both flexible joints and body approach [4].

The flexible joints and rigid body approach is an effective tool for dynamic modeling of the machine tools. The advantages in terms of computing time justify the application of this method in many researches, where dynamic behavior is mainly influenced by low-frequency dominant modes and the rigidity of the joints are weak compared to the rigidity of the links [4, 7].

Pan et al. [7] and Rafieian [8] studied instability phenomena in robotic machining based on flexible joints and rigid body approach. Based on this modeling approach, only low frequencies for the robot, depending on joint flexibility, can be obtained. This modeling approach does not allow determining the high-frequency range that is needed for analyzing stability of robotic machining equipped with a high-speed spindle.

Machine tool structures are more rigid than the serial robots, and their bodies can be assumed as infinitely rigid. However, considering the robot links as infinitely rigid is not adapted for accurate prediction because they are not rigid enough as machine tool parts [4, 9].

Mousavi et al. [4] studied two modeling approaches and compared them according to their respective capabilities to predict machining stability. This comparison demonstrates the necessity of considering link flexibilities for stability analysis in robotic machining.

In order to consider the flexibility of robot links, the finite element method (FEM) can be used. It provides an accurate

estimation of static behavior by the determination of the robot stiffness matrix in the workspace [9–11]. Variation in robot dynamic behavior can be tracked along a machining trajectory by several frequency-domain simulations of local linearized FEM. Time-domain simulation of nonlinear FEM is impracticable due to the high model complexity and calculation cost [9].

Matrix structural analysis (MSA) method [11, 12], as a simplified FEM, uses equivalent beam elements for the modeling of mechanical structure components. It is used for model reduction. This method has been applied to predict the dynamic behavior of machine tool parts such as spindle rotors using Timoshenko beam elements [3], as well as complete machine tools using Bernoulli beam elements [12]. This method enables the analysis of the dynamic behavior of a robot in different configurations along a machining trajectory with an acceptable computing time.

In section 2, the MSA method is used to elaborate a reduced, but enough accurate dynamic model of the STAUBLI 170 BH industrial machining robot by considering the flexibility of links. In section 3, the parameters of the robot dynamic model are identified on the basis of experimental results [13–15]. This model is used in section 4 to predict stability conditions, according to the configurations of the robot. The stability limits are established as a function of the kinematic redundancy variable. The experimental tests of machining operations are realized and confirm the dynamic model predictions. Finally, conclusions are presented in section 5.

2 Dynamic model of the STUBLI 170 BH robot

Dynamic modeling and simulations along a machining trajectory by using FEM of the real robot body geometries is ineffective because of the large size of the resulting models and the high computational time. In this paper, the MSA method is used to reduce model size and, consequently, the calculation

time of simulation process along a machining trajectory. To this end, each link of the robot structure is represented by three-dimensional (3D) Euler–Bernoulli beam elements as shown in Fig. 2.

The 3D beam element has two nodes and 12° of freedom. The nodal displacements in the local frame are arranged as

$$\boldsymbol{U}_{Local} = \left[u_1\ v_1\ w_1\ \theta_{x1}\ \theta_{y1}\ \theta_{z1}\ u_2\ v_2\ w_2\theta_{x2}\ \theta_{y2}\ \theta_{z2}\right]^T$$

The displacement transformation matrix between local and global coordinates is

$$\boldsymbol{U}_{Local} = \boldsymbol{Q} \cdot \boldsymbol{U}_{Global} \tag{1}$$

where $\boldsymbol{Q}$ is the local to the global coordinate transformation matrix. It is a 12×12-block orthogonal matrix which is obtained in the local coordinate direction cosines expressed in the global one. The direction cosines of the local coordinate

attached to the beam i (X_i, Y_i, and Z_i) in the global coordinate (X_0, Y_0, and Z_0) (Fig. 2) are presented as shown in Table 1.

The transformation matrix for element i then is written as

$$[\boldsymbol{Q}_i]_{12\times12} = \begin{bmatrix} \lambda & 0 & 0 & 0 \\ 0 & \lambda & 0 & 0 \\ 0 & 0 & \lambda & 0 \\ 0 & 0 & 0 & \lambda \end{bmatrix}_{12\times12} \tag{2}$$

where $[\boldsymbol{\lambda}]_{3\times3} = [l_1\quad m_1\quad n_1\ l_2m_2n_2\ l_3m_2n_3]$

The same transformation is used for nodal force.

$$\boldsymbol{F}_{Local} = \boldsymbol{Q} \cdot \boldsymbol{F}_{Global} \tag{3}$$

Thereafter, the principle of virtual displacements in local frame is

$$\boldsymbol{F}_{Local} = \boldsymbol{K}_q \cdot \boldsymbol{U}_{Local} \tag{4}$$

where $\boldsymbol{K}_q$ is the stiffness matrix of the element in the local coordinate. The results are recalled here for the 3D case:

$$\boldsymbol{K}_q = \begin{bmatrix}
\frac{EA}{L} & 0 & 0 & 0 & 0 & 0 & \frac{-EA}{L} & 0 & 0 & 0 & 0 & 0 \\
0 & \frac{12EI_z}{L^3} & 0 & 0 & 0 & \frac{6EI_z}{L^2} & 0 & \frac{-12EI_z}{L^3} & 0 & 0 & 0 & \frac{6EI_z}{L^2} \\
0 & 0 & \frac{12EI_y}{L^3} & 0 & \frac{-6EI_y}{L^2} & 0 & 0 & 0 & \frac{-2EI_y}{L^3} & 0 & \frac{-6EI_y}{L^2} & 0 \\
0 & 0 & 0 & \frac{GI_x}{L} & 0 & 0 & 0 & 0 & 0 & -\frac{GI_x}{L} & 0 & 0 \\
0 & 0 & \frac{-6EI_y}{L^2} & 0 & \frac{4EI_y}{L} & 0 & 0 & 0 & \frac{6EI_y}{L^2} & 0 & \frac{2EI_y}{L} & 0 \\
0 & \frac{6EI_z}{L^2} & 0 & 0 & 0 & \frac{4EI_z}{L} & 0 & \frac{-6EI_z}{L^2} & 0 & 0 & 0 & \frac{2EI_z}{L^2} \\
-\frac{EA}{L} & 0 & 0 & 0 & 0 & 0 & \frac{EA}{L} & 0 & 0 & 0 & 0 & 0 \\
0 & \frac{12EI_z}{L^3} & 0 & 0 & 0 & \frac{-6EI_z}{L^2} & 0 & \frac{12EI_z}{L^3} & 0 & 0 & 0 & \frac{-6EI_z}{L^2} \\
0 & 0 & \frac{-12EI_y}{L^3} & 0 & \frac{6EI_y}{L^2} & 0 & 0 & 0 & \frac{12EI_y}{L^3} & 0 & \frac{6EI_y}{L^2} & 0 \\
0 & 0 & 0 & \frac{-GI_x}{L} & 0 & 0 & 0 & 0 & 0 & \frac{GI_x}{L} & 0 & 0 \\
0 & 0 & \frac{-6EI_y}{L^2} & 0 & \frac{2EI_y}{L} & 0 & 0 & 0 & \frac{6EI_y}{L^2} & 0 & \frac{4EI_y}{L} & 0 \\
0 & \frac{6EI_z}{L^2} & 0 & 0 & 0 & \frac{2EI_z}{L} & 0 & \frac{-6EI_z}{L^2} & 0 & 0 & 0 & \frac{4EI_z}{L}
\end{bmatrix}$$

It can be written in the global coordinate as

$$\boldsymbol{F}_{Global} = \boldsymbol{K}_x \cdot \boldsymbol{U}_{Global} \tag{5}$$

where $\boldsymbol{K}_x$ is the stiffness matrix in the global coordinate. Hence, stiffness matrix in the global coordinate is obtained through the congruent transformation (the transformation
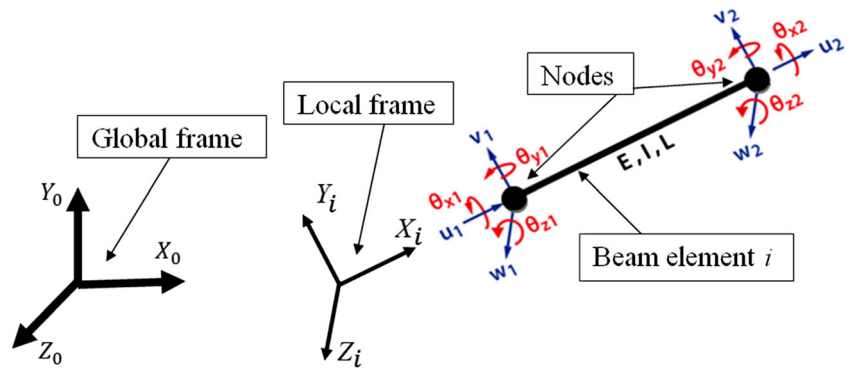
matrix is orthogonal: $\boldsymbol{Q}^{-1} = \boldsymbol{Q}^T$).

$$\boldsymbol{K}_x = \boldsymbol{Q}^T \cdot \boldsymbol{K}_q \cdot \boldsymbol{Q} \tag{6}$$

Similarly, mass and damping matrices in the global frame are written as

$$X_x = \boldsymbol{Q}^T X_q \boldsymbol{Q} \quad \text{with } X = \boldsymbol{M}, \boldsymbol{K}, \boldsymbol{C} \tag{7}$$

Fig. 2 3D beam elements with 12° of freedoms

The global mass and stiffness matrices of the structure are obtained by assembling the mass and stiffness of the structure elements in the global coordinate.

A simplified beam element model of the STAUBLI 170 BH robot is developed on MATLAB® as shown in Fig. 3b. The STAUBLI 170 BH serial industrial robot is composed of six active joint q = [q1…q6] and six links as shown in Fig. 3. It is equipped with a high spindle speed.

The Travel Coordinate System (TCS) type model is applied to identify the local frame in the kinematic chain as illustrated in Fig. 4 [16].

Two characteristic dimensions of the kinematic element i are axial offset a_i, measured on the axis of the pair (i-1, i) ($O_iO_{i''}$), and link length b_i, defined by the normal to the axes of the two pairs adjacent to element i ($O_{i''}O_{i'}$) (Fig. 4). These parameters are determined from the actual geometry of the robot as presented in Table 2.

The direct geometric model defining the pose of the end-effector in the global frame is represented by the following transformation from $O_0X_0Y_0Z_0$ (global coordinate) to $O_6X_6Y_6Z_6$ (local frame attached to end-effector) [16, 17]:

$$O_0X_0Y_0Z_0 \xrightarrow{R^X_{01}(\varphi_{10})} O_1X_1Y_1Z_1 \xrightarrow{T^Z_{11'}(b_1)} O_{1'}X_{1'}Y_{1'}Z_{1'} \xrightarrow{R^Y_{1'2}(\varphi_{21})} O_2X_2Y_2Z_2$$

$$\xrightarrow{T^Y_{22''}(a_2)} O_{2''}X_{2''}Y_{2''}Z_{2''} \xrightarrow{T^X_{2''2'}(b_2)} O_{2'}X_{2'}Y_{2'}Z_{2'} \xrightarrow{R^Y_{2'3}(\varphi_{32})} O_3X_3Y_3Z_3 \xrightarrow{R^Y_{34}(\varphi_{43})} O_4X_4Y_4Z_4 \xrightarrow{T^Z_{44''}(a_4)} O_{4''}X_{4''}Y_{4''}Z_{4''} \xrightarrow{R^X_{4'5}(\varphi_{54})} O_5X_5Y_5Z_5$$

$$\xrightarrow{T^Y_{55''}(a_5)} O_{5''}X_{5''}Y_{5''}Z_{5''} \xrightarrow{R^Y_{5''6}(\varphi_{65})} O_6X_6Y_6Z_6$$

In these transformations, $\overrightarrow{R^a_{bc}}(\varphi)$ denotes a homogeneous 4×4 matrix associated to a rotation of angle φ around the axis $\overrightarrow{a}$ (X, Y or Z) from the local coordinate b ($O_iX_iY_iZ_i$) to the local coordinate element c ($O_{i+1}X_{i+1}Y_{i+1}Z_{i+1}$). $\overrightarrow{T^e_{fg}}(d)$ denotes a homogeneous 4×4 matrix to a linear transformation matrix along the axis $\overrightarrow{e}$ (X, Y or Z) from the local coordinate f ($O_iX_iY_iZ_i$) to the local coordinate g ($O_{i'}X_{i'}Y_{i'}Z_{i'}$ or $O_{i''}X_{i''}Y_{i''}Z_{i''}$) by a displacement of d (a_i or b_i presented in Table 2).

A_{06} is an operator defining the pose, and the end-effector is expressed as follows [17]:

$$A_{06} = \underbrace{R^X_{01}(\varphi_{10}).T^Z_{11'}(b_1)}_{A_{01}} \cdot \underbrace{R^Y_{1'2}(\varphi_{21}).T^Y_{22''}(a_2).T^X_{2'2'}(b_2)}_{A_{12}} \cdot \underbrace{R^Y_{2'3}(\varphi_{32})}_{A_{23}} \cdot \underbrace{R^Y_{34}(\varphi_{43}).T^Z_{44''}(a_4)}_{A_{34}} \cdot \underbrace{R^X_{4'5}(\varphi_{54})T^Y_{55''}(a_5)}_{A_{45}} \cdot \underbrace{R^Y_{5''6}(\varphi_{65}).T^X_{66''}(a_6)}_{A_{56}}$$

Otherwise,

$$A_{06} = \prod_{i=1}^{6} A_{i-1,i} = A_{01}A_{12}A_{23}A_{34}A_{45}A_{56}$$

where $A_{i-1,i}$ is the 4×4 homogenous matrix that expresses the position and the orientation of the local frame of element i relative to the local frame of element i-1. The local frame of a robot element (i) relative to the global frame is obtained as follows:

$$A_{0i} = \prod_{k=1}^{i} A_{k-1,k} = \begin{bmatrix} 0 & 0 & 0 & 1 \\ X_i & & & \\ Y_i & & [\lambda_{Oi}]_{3\times3} & \\ Z_i & & & \end{bmatrix}$$

Table 1 Direction cosines between axes

	x_i	y_i	z_i
X_0	l_1	m_1	n_1
Y_0	l_2	m_2	n_2
Z_0	l_3	m_3	n_3

The homogenous matrix orientation part ($\boldsymbol{\lambda}_{0i}$) is used to determine the transformation matrix of each robot element (Eq. 2).

To define the inverse geometric model of the robot, Paul's method [18] is used. The inverse geometric model gives the different joint variables ($\varphi_{i,i-1}$) according to the known end-effector poses A_{06} along a machining trajectory.

Based on the MSA method, each robot's link is represented by a 3D beam element (Fig. 3b) and assembled by following the flow chart shown in Fig. 5. Elementary matrices are assembled in the global coordinate system as in the classic finite element procedure.
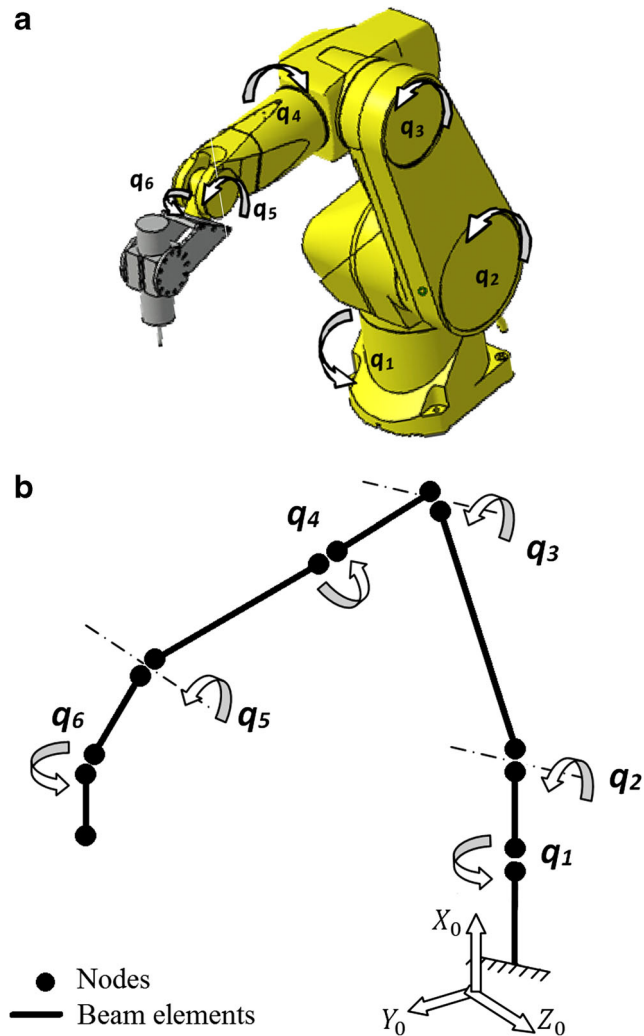
Fig. 3 a Stäubli 170 BH CAD model; **b** beam elements model of the robot

3 Identification of robot parameters

The flexible joints are modeled by linear torsional springs. The joint stiffness values for the STAUBLI 170 BH robot were obtained experimentally by Olabi et al. [19] based on the measurement of joint angular displacements due to the static load. The joint stiffness values from the base to the end-effector respectively are presented in Table 3.

A linearized dynamic model of the robot, for a given configuration x_0 in the global frame, can be expressed by the following differential equation:

$$\boldsymbol{M}_x(x_0)\ddot{\delta}_x(t) + \boldsymbol{C}_x(x_0)\dot{\delta}_x(t) + \boldsymbol{K}_x(x_0)\delta_x(t) = \boldsymbol{F}(t) \qquad (8)$$

where $\delta_x(t) = x(t) - x_0$ is an infinitesimal nodal displacement relative to the global frame. $\boldsymbol{F}(t)$ is the force vector. $\boldsymbol{M}_x$, $\boldsymbol{C}_x$, and $\boldsymbol{K}_x$ are respectively robot system mass, damping, and stiffness matrices in the global frame. They are determined for each configuration in the robot workspace according to the flow chart given in Fig. 5.

The beam element's dimensions are determined from CAD models supplied by the robot manufacturer as presented by Oueslati et al. [14]. The equivalent Young modulus of the robot is identified to $E_{Alu} = 69.10^9 pa$, and the equivalent density is $\rho_{Alu} = 2700\ Kg/m^3$ [14].

In dynamic analysis of structures, damping plays an important role. The experimental identification carried out by Mejri et al. [5] enables the determination of the actual modal parameters of the robot structure in a given position and configuration where the tests are performed. It is not valid for other positions and configurations of the robot, but they are usually required as an effective means to calibrate numerical models. Swiatek et al. [20] performed the numerical identification of damping which is carried out by using FEM simulation with ADAMS®. This damping model remains a numerical approximation. Proportional damping occurs in most industrial cases. It is the most common approach to model dissipative forces in complex engineering structures. It can be easily integrated into Altintas formulation for identification of the stability limit.

The proportional damping model expresses the damping matrix ($\boldsymbol{C}_x$) as a linear combination of the mass ($\boldsymbol{M}_x$) and stiffness matrices ($\boldsymbol{K}_x$) (Rayleigh hypothesis) [21], that is,

$$\boldsymbol{C}_x = \alpha \boldsymbol{M}_x + \beta \boldsymbol{K}_x \qquad (9)$$

α and β values are determined by using vibration testing. The major advantage to consider proportional damping lies on the fact that a structure having n degrees of freedom can be represented by n uncoupled real mode [22]. For this reason, the damping in the form shown in Eq. 9 is advantageous as an

Fig. 4 Robot structural diagram with the TCS model notation
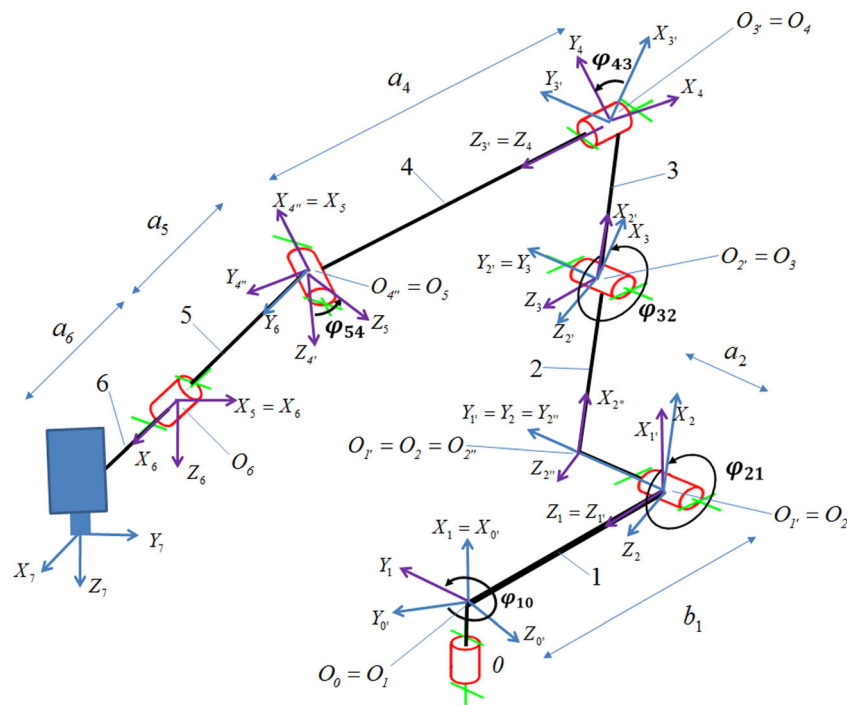
orthogonal transformation, and the damping term in Eq. 8 reduces to

$$[P]^T \cdot [C_x] \cdot [P]$$

$$= \begin{bmatrix} \alpha + \beta\omega_1^2 & 0 & . & . & 0 \\ 0 & \alpha + \beta\omega_2^2 & . & . & . \\ . & . & . & . & . \\ . & . & . & \alpha + \beta\omega_k^2 & . \\ 0 & . & . & . & \alpha + \beta\omega_n^2 \end{bmatrix}_{n \times n}$$

(10)

where $[P]$ is the eigenvector matrix and ω_{0k} is the kth natural frequency of the structure. Again, from symmetry, it can be inferred that, as it is shown in Eq. (11), the orthogonal transformation of the damping ration matrix reduces to the form [22]

$$\xi_k = \frac{1}{2}\left(\alpha\omega_{0k} + \frac{\beta}{\omega_{0k}}\right)$$

(11)

Bearee [15] realized the experimental test on STAUBLI 170 BH robot for two different configurations. For the first

configuration, the estimated dominating frequency is 8.2 Hz and 5.9 Hz for the second one. The damping ratio associated with this mode is estimated for both configurations at 6.5 %. Hence, these results are used to determine damping matrix coefficient values (α and β) using the damping ratio for k^{th} mode (ξ_k).

The natural frequencies and mode shapes of the robot system are determined numerically as solutions of the following Eigen problem equations:

$$\left(K_x - \omega_{0k}^2 M_x\right)P_k = 0$$

(12)

where P_k is the kth mode shape (eigenvector) of the robot structure. It has a nontrivial solution if and only if

$$\det\left(K_x - \omega_{0k}^2 M_x\right) = 0$$
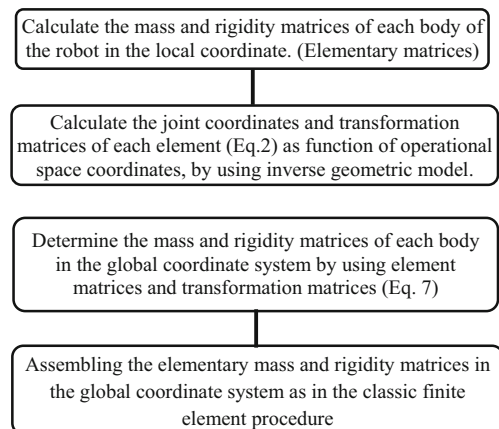
Fig. 5 Chart flow to construct a FE model of the robot in any configuration in the workspace

Table 2 Geometrical parameters of the Stäubli RX 170 B robot [14]

Element i	a_i (mm)	b_i (mm)
1	0	100
2	70	0
3	0	0
4	750	0
5	135	0
6	200	0

Table 3 Joints stiffness of the STAUBLI 170 BH serial robot [19]

| Axis	1	2	3	4	5	6
K (N.m/rad)	2.04×10^5	1.75×10^6	5.7×10^5	4.9×10^5	1.2×10^5	0.05×10^5

Due to changes in robot posture along a machining trajectory, as shown in Fig. 6, the dynamic behavior of the robot and the natural frequencies vary within its workspace.

The considered machining trajectory is a linear trajectory in the Y_0 direction from $y = 0.4 m$ to $y = 1.5\ m$ for a constant value of $x = 0.1\ m$. Natural frequencies of the robot for different end-effector positions along the machining trajectory can be obtained by following the chart presented in Fig. 5 and solving Eq. 12 for each robot configuration. Variations in natural frequencies along the considered trajectory are shown in Fig. 7.

It can be seen that the natural frequencies of the robot have a wide range of low frequency (5 Hz) to high frequency (10 kHz). The natural frequencies can vary up to 40 % along the simple linear trajectory. Therefore, these dynamic behavior variations must necessarily be taken into account in stability analysis. The machining operation can be in stable condition at the starting point of the machining trajectory, then in unstable condition during operation.

On the other hand, these variations related to the robot configuration provide to take advantage of kinematic redundancy in robotic machining. The next section studies this possibility in robotic machining.

A dynamic model to predict the robot dynamic behavior along a machining trajectory in its workspace has been elaborated in this section. Thus, the stability prediction in robotic machining can be studied.
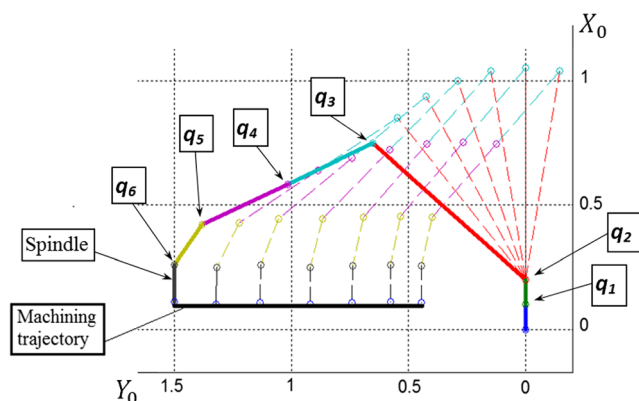
Fig. 6 Different configurations of the robot along the machining trajectory

4 Stability prediction

A stability diagram based on regenerative chatter theory is an effective tool to predict and control chatter vibrations. The stability diagram of a machining process represents the interaction between structural dynamics and the cutting process. It is determined by solving the closed loop block diagram (Fig. 1a). Based on the milling theory proposed by Budak and Altintas [2], the cutting force model in milling operations can be written in the form [23, 24]

$$F(t) = \frac{1}{2} K_c D(t) b [\delta(t) - \delta(t - \tau)] \tag{13}$$

where K_c is the specific cutting pressure matrix, τ is the tooth passing period of the cutting tool, b is the depth of cut (Fig. 8), and $[\delta(t) - \delta(t - \tau)]$ are the tool tip displacement vectors due to vibration at the current time (t) and previous tooth period ($t - \tau$). $D(t)$ represents time-variant directional dynamic milling force coefficients. It can be expanded into a Fourier series, and the most simplistic approximation is its average component D_o [2].

$$D_0 = \frac{N}{2\pi} \begin{bmatrix} \alpha_{xx} & \alpha_{xy} \\ \alpha_{yx} & \alpha_{yy} \end{bmatrix}$$

where time-variant directional dynamic milling force coefficients are given as

$$a_{yy} = \frac{1}{2} [\cos 2\varnothing - 2r\varnothing + r\sin 2\varnothing]_{\varnothing_{st}}^{\varnothing_{ex}}$$

$$a_{yz} = \frac{1}{2} [-\sin 2\varnothing - \varnothing + r\cos 2\varnothing]_{\varnothing_{st}}^{\varnothing_{ex}}$$

$$a_{zy} = \frac{1}{2} [-\sin 2\varnothing + 2\varnothing + r\cos 2\varnothing]_{\varnothing_{st}}^{\varnothing_{ex}}$$

$$a_{zz} = \frac{1}{2} [-\cos 2\varnothing - 2r\varnothing - r\sin 2\varnothing]_{\varnothing_{st}}^{\varnothing_{ex}}$$

where r is the ratio of radial and tangential specific cutting pressure and $\varnothing_{st}$ and $\varnothing_{ex}$ are the start and exit angles of the cutting tooth as illustrated in Fig. 8.

Substituting the harmonic solution $\delta(t)$: $\delta(t) = \Delta e^{i\omega t}$ into the cutting force equation (Eq. 13) and then into the motion equation (Eq. 8) gives

$$[-M\omega^2 + C\omega i + K]\Delta = \frac{1}{2} K_c D_0 b (1 - e^{-i\omega\tau})\Delta \tag{14}$$
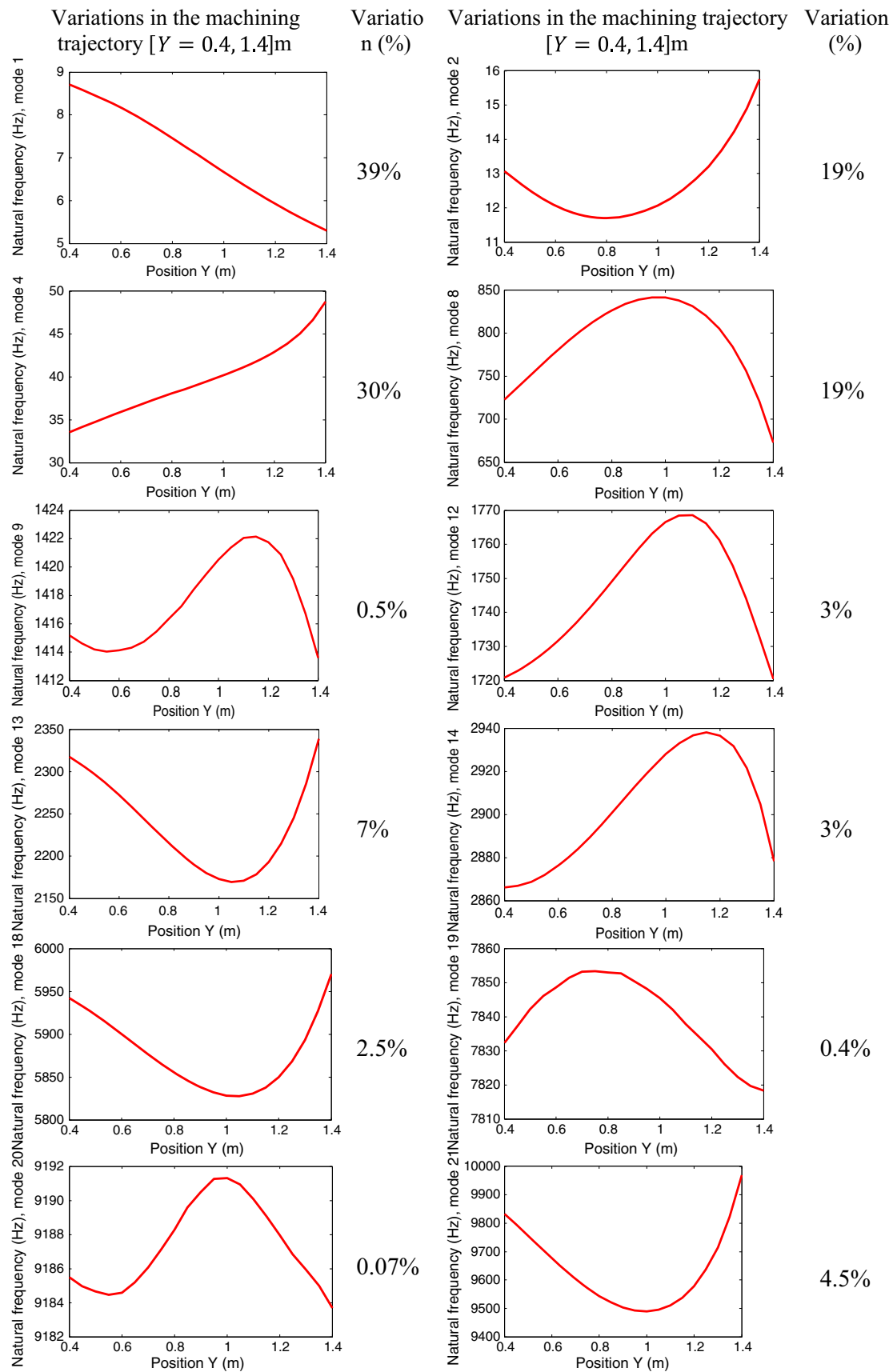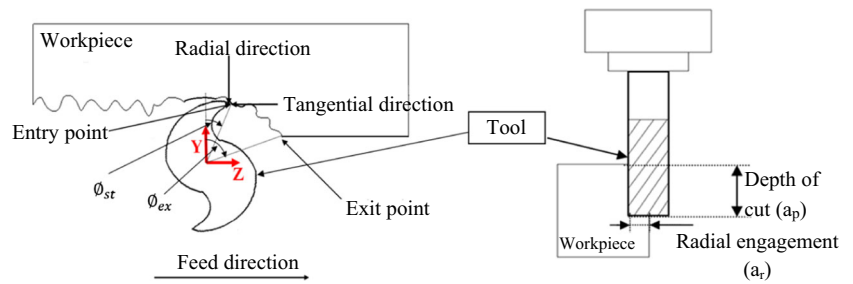
Fig. 7 Variation of natural frequencies along the considered machining trajectory

Fig. 8 Cutting parameters in milling

In addition, the transfer function of the structure is

$$H(\omega) = \left[-M\omega^2 + iC\omega + K \right]^{-1}$$

By substituting the transfer function into Eq. 14,

$$\left[I - \frac{1}{2} K_c D_0 b \left(1 - e^{-i\omega\tau} \right) H(\omega) \right] \Delta = 0 \qquad (15)$$

This equation has a nontrivial solution if the determinant below is zero:

$$det \left[I - \frac{1}{2} K_c D_0 b \left(1 - e^{-i\omega\tau} \right) H(\omega) \right] = 0 \qquad (16)$$

The oriented transfer function matrix is defined by $D_0 H(\omega)$; ; thus, the eigenvalues of the characteristic equation (Eq. 16) at specific chatter vibration frequencies $\omega = \omega_c$ are given by

$$\Lambda = \Lambda_R + \Lambda_I = -\frac{N}{4\pi} b K_c \left(1 - e^{-i\omega_c\tau} \right) \qquad (17)$$

N is the number of tool teeth. By solving Eq. 17 and determining the characteristic equation for b, the imaginary part of b is equal to zero and gives the time delay between the passage of consecutive tool teeth (τ). The real part of b gives the depth-of-cut limit (b_{lim}) in chatter frequency (ω_c), which separates the stability and instability zones [2, 23]. After some manipulations, the stability limit (b_{lim}) can be written as

a

b
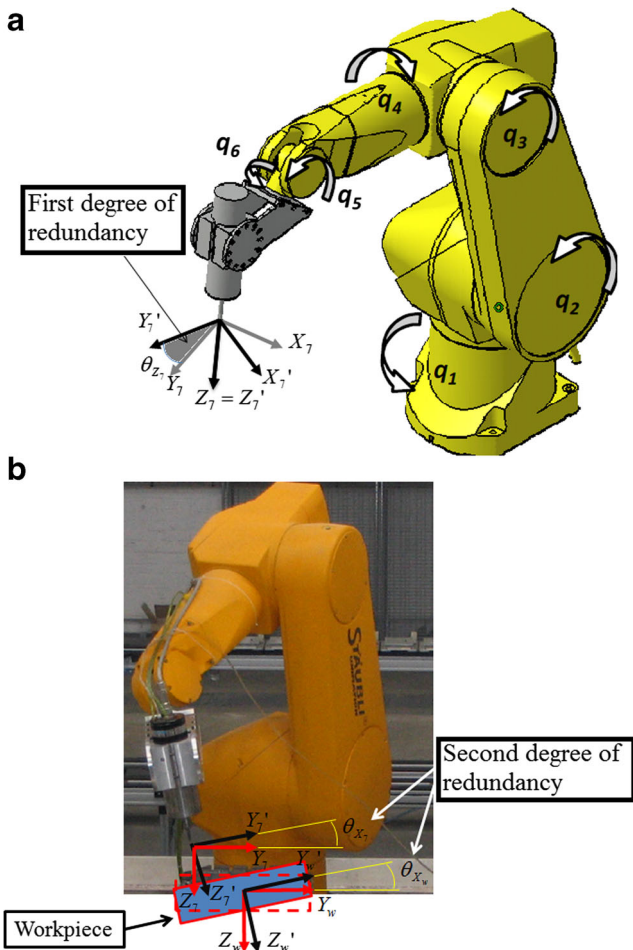
Fig. 9 **a** First functional redundancy ; **b** second functional redundancy
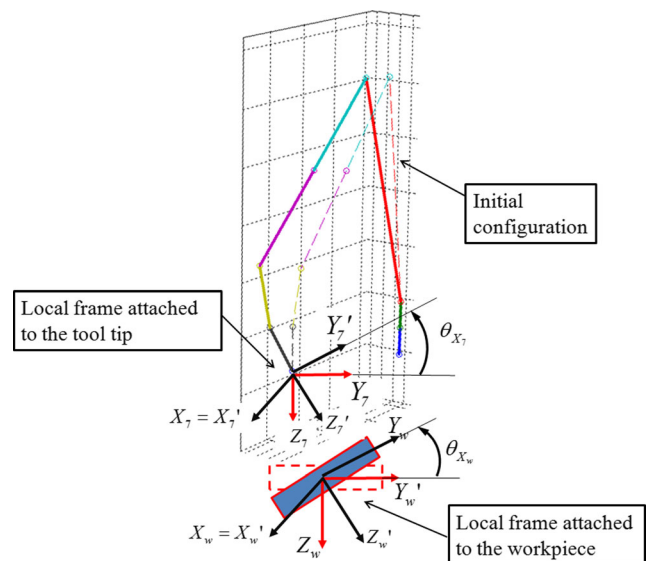
Fig. 10 Tool tip rotation around X_7 in the local frame

Table 4 Cutting parameters

Milling tool	Tia1N ϕ 8mm, 6 dents	
Axial depth of cut (ap)	1.5 mm	
Spindle Speed	4000 rpm	
Feed	1680 mm/min	
Radial engagement (ae)	1.2 mm	

$$b_{lim} = -\frac{2\pi \Lambda_R}{NK_t}\left(1 + \kappa^2\right) \qquad (18)$$

where κ is defined as

$$\kappa = \frac{\Lambda_I}{\Lambda_R} = \frac{sin\omega_c\tau}{1-cos\omega_c\tau}$$

4.1 Stability prediction in machining robot

One of the advantages of robotic machining is taking advantage of the kinematic redundancy. This means that for the same machining trajectory, different robot configurations are possible. Because of this, kinematic redundancy has been the subject of many robotic optimization studies. Different criteria are defined to manage redundancy, such as stiffness improvement [17], accuracy, etc. In this paper, the distance from the stability limit is the criteria to optimize robot poses in machining.

A serial robot manipulator has functional redundancy when the operational space dimension n_o is larger than the degree t of the task performed. The degree of functional redundancy is determined as follows [25]:

$$r_f = n_o - t \qquad (19)$$

A one-axis rotary table is integrated into the robotic cell. The table rotates around Y_0 in the global frame. In certain machining

operations, such as drilling, face milling, plunge milling, etc., the cutting tool axis could be perpendicular to the machined surface. Hence, the machining task degree (t) is five (three positions and two rotations). In this robotic cell, formed by the STAUBLI 170 BH robot with six active joints and external rotary table with one axis, the degree of freedom $n_o = 6 + 1$ and the degree of functional redundancy $r_f = 2$. These redundancies allow us to have an infinite number of configurations for a given position of the end-effector in the task space (relative to the workpiece). The set of these configurations forms the internal motion space. The first internal motion is the spindle rotation around the Z_7 axis of the local frame ($X_7 Y_7 Z_7$) attached to the tool tip as shown in Fig. 9a. The second one consists in the rotation of the end-effector and the table as if they were a single rigid body around the X_w axis of the local frame ($X_w Y_w Z_w$) attached to the workpiece to keep tool axis perpendicular to the machined surface as shown in Fig. 9b.

Hence, for the same tool position, different solutions for the value of angles θ_{Xw} and θ_{Z7} are possible (Figs. 9 and 10). Therefore, unlimited configurations can be considered. Each robot configuration has its own dynamic behavior and stable cutting conditions. Thus, this robot property enables us to optimize robot configurations regarding machining stability conditions using redundancy in robotic machining.
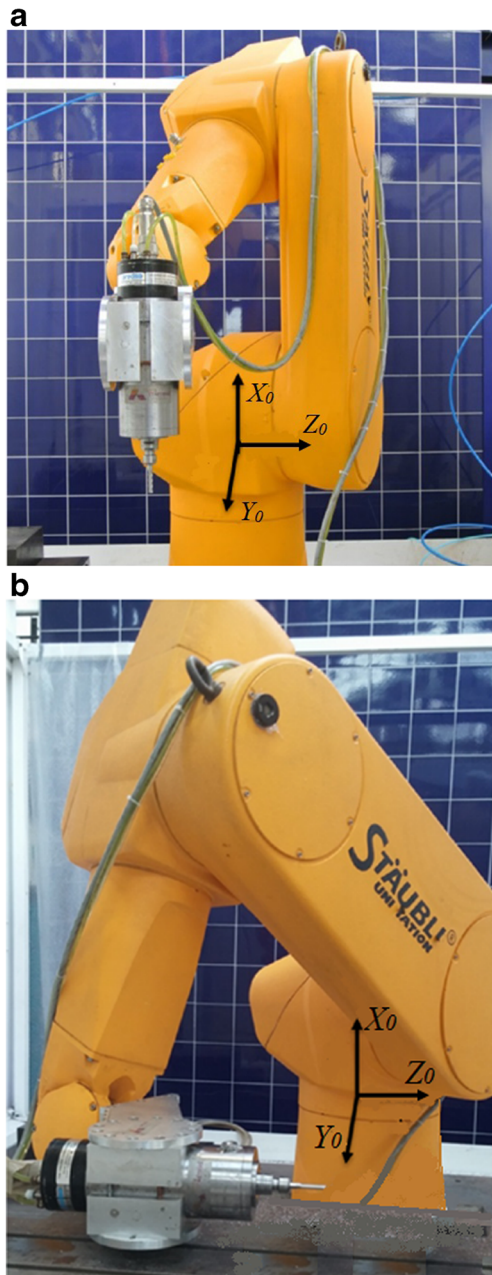
In this section, the second redundancy is studied. To this end, the spindle rotates around the X_7 axis with a value for θ_{X7} without changing the tool tip position. At the same time, the workpiece rotates around the X_w axis with a value for θ_{Xw} in

Fig. 11 Stability prediction and selected experimental configuration
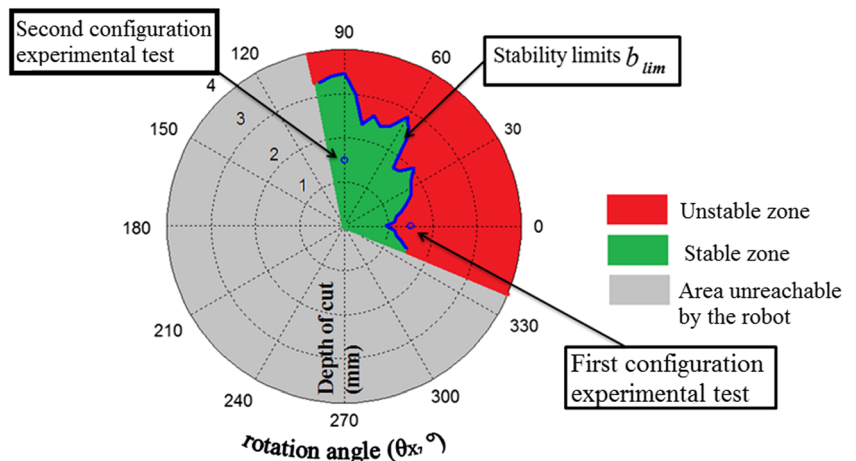
order to maintain the tool axis perpendicular to the machined surface (Fig. 10). The local frames in the new configuration are represented by (X'_7, Y'_7, Z'_7) and (X'_w, Y'_w, Z'_w) as shown in Figs. 9 and 10.

By following the chart presented in Fig. 5 and using Eq. 18, for each configuration, a stability limit can be determined. The stability limits from the numerical model (developed in section 2) is established for different possible configurations using the second redundancy θ_{X7} (Fig. 10). Machining is considered milling operation on an aluminum workpiece with cutting parameters presented in Table 4.

Therefore, the robot configuration varies in the internal motion space when θ_{X7} is considered as a redundant kinematic parameter. The stability diagram as a function of structure rotation angle around the X_w axis (θ_{X7}) and the depth of cut are presented in Fig. 11.

The predicted stability limits are established for the cutting parameters presented in Table 4. Stable and unstable zones are dependent on the machining parameters (Table 4) such as spindle speed or feed and radial depth of cut.

To compare stability diagram results with experimental tests, two configurations are selected based on the theoretical stability diagram shown in Fig. 11. For the same cutting conditions, the first configuration is in unstable zone and the second one is in stable zone. These two selected configurations are illustrated in Fig. 12a, b.

4.2 Experimental results

Experimental machining testes are carried out with the STAUBLI 170 BH industrial manipulator by Olabi et al.

Fig. 12 **a** First configuration with $\theta_{X7} = 0°$; **b** second configuration with $\theta_{X7} = 90°$
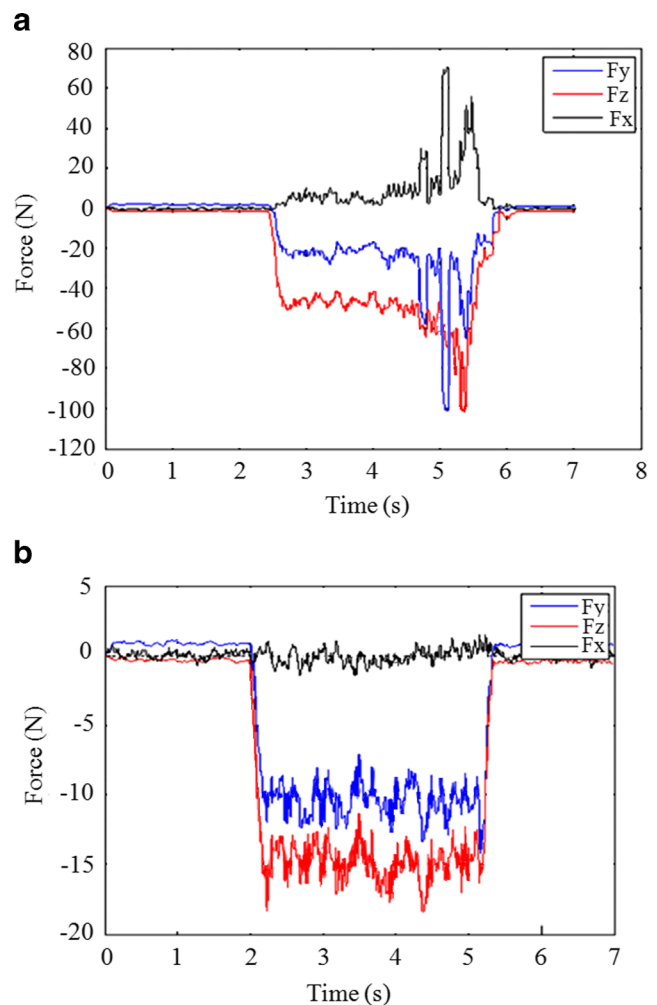
Fig. 13 The forces measured in the machining operation by **a** first configuration and **b** second configuration [13]

[13] in two configurations selected in Fig. 11 and shown in Fig. 12. Experimental cutting tests are performed on aluminum workpieces fixed on a force measurement table with the cutting parameters presented in Table 4.

Figure 13 presents the cutting forces measured during the considered machining operation. In Fig. 13a, we can observe that the cutting force variations grow suddenly which means instability in the machining operation (chatter). The machining marks clearly reflected the chatter vibrations marks on the workpiece [13].

The numerical stability limit diagram (Fig. 11) clearly illustrated that the first configuration is in unstable zone. The experimental machining in the second configuration gives a stable condition (Fig. 13b). The numerical results (Fig. 11) also predicted that the second robot configuration has a maximum distance from unstable zone. The cutting parameters were the same for two experimental machining tests, but the robot configuration changes using the redundancy which modifies the stability condition.

Applying this method for all points of a machining trajectory allows the robot configuration to be optimized against instability condition and to maximize stability margins in order to maintain productivity performance.

5 Conclusion

The principal objective of this work is to develop a numerical model to predict the dynamic behavior of robotic manipulator in a machining operation. This model enables stability limits to be determined along machining trajectories. Hence, a numerical model of the STAUBLI 170 BH industrial machining robot is elaborated by using 3D Euler–Bernoulli beam elements based on the matrix structural analysis method. The numerical model is readjusted by experimental results realized at the specific positions. The numerical model enables to predict the robot's dynamic behavior as well as stability limits with respect to posture change along a machining trajectory in the robot workspace.

The proposed stability diagram shows the variations of the robot dynamic behavior in the internal motion space for the same cutting parameters and the same trajectory position as a function of robot redundancy. This stability limit enables to predict the robot configuration for which machining operations are at a maximum stable margin. The prediction from the theoretical stability limit diagram is consistent with the observations obtained from experimental cutting results. The numerical model and machining results confirm that the stability in robotic machining can be ensured by managing functional redundancy in order to maintain productivity without changing the cutting parameters.

This prediction approach can be applied to all points of a machining trajectory in order to optimize the robot configurations regarding stability through functional redundancy control.

In this paper, exploitation of kinematic redundancy has been performed for a serial industrial robot. This approach can be applied to other kinematic architectures of robots: serial, parallel, and hybrid.

References

1. Tobias SA, Fishwick W (1958) The chatter of lath tools under orthogonal cutting conditions. ASME 1079–1088.
2. Altintas Y (2000) Manufacturing automation. Metal cutting mechanics, machine tool vibrations and CNC design, Cambridge University Press
3. Mousavi S, Gagnol V, Ray P (2013) Machining prediction of spindle–self-vibratory drilling head. J Mater Process Technol 213(12): 2119–2125
4. Mousavi S, Gagnol V, Bouzgarrou BC, Ray P (2013) Dynamic behavior model of a machining robot and stability prediction, ECCOMAS, Zagreb
5. Mejri S, Gagnol V, Phu Le T, Ray P, Paultre P (2015) Dynamic characterization of machining robot and stability analysis. Int J Adv Manuf Technol
6. Gagnol V, Bouzgarrou BC, Ray P, Barra C (2007) Model-based chatter stability prediction for high-speed spindles. Int J Mach Tools Manuf 47(7):1176–1186
7. Pan Z, Zhang H, Zhu Z, Wang J (2006) Chatter analysis of robot machining process. J Mater Process Technol 173:301–309
8. Rafieian F, Hazel B, Liu Z (2014) Regenerative instability of impact-cutting material removal in the grinding process performed by a flexible robot arm, 6th CIRP International Conference on High Performance Cutting, HPC2014, Procedia CIRP 14:406–411
9. Maglie P (2012) Parallelization of design and simulation. Virtual machine tools in real product development. VDI Verlag GmbH (2012), theses, Department of Mechanical and Process Engineering, Düsseldorf
10. Bouzgarrou BC, Fauroux JC, Gogu G, Heerah Y. Rigidity analysis of T3R1 parallel robot with uncoupled Kinematics
11. Ruggiu M (2012) Cartesian stiffness matrix mapping of a translational parallel mechanism with elastic joints. Int J Adv Robot Syst 9
12. Kessentini A, Chevalier G, Louati J, Rivière A, Haddar M (2007) F.E.M. of the drilling machine-tool including the gyroscopic effect. Adv Prod Eng Manag 2:63–78
13. Olabi A, Bearee R, Thomas O, Gibaru O, Gonzalez J (2014) Analyse expérimentale des phénomènes vibratoires d'un robot usineur. MUGV
14. Oueslati M, Gibaru O, Bearee R, Moraru G (2013) Contribution à la modélisation dynamique, l'identification et la synthèse de lois de commande adaptées aux axes flexibles d'un robot industriel. Theses, Paris Tech
15. Bearee R (2014) New Damped-Jerk trajectory for vibration reduction. Control Eng Pract 28:112–120

16. Gogu G, Coiffet P, Barraco A (1997) Representation of robots displacements, Paris :Hermes
17. Subrin K, Sabourin L, Cousturier R, Gogu G, Mezouar Y (2012) Performance criteria to evaluate a kinematically redundant robotic cell for machining tasks. Appl Mech Mater 162:413–422
18. Paul RP (1981) Robot manipulators: mathematics, programming, and control: the computer control of robot manipulators, Richard Paul
19. Olabi A, Bearee R, Damak M, Gibaru O (2010) Mouvement à rigidité maximale pour un robot 6 axes destiné à des opérations d'usinage. MUGV
20. Swiatek G, Liu Z, Hazel B (2010) Dynamic simulation and configuration dependant model identification of a portable flexible-link and flexible-joint robot, 28th seminar on machinery vibration. 189–206
21. Adhikari S (2006) Damping modelling using generalized proportional damping. J Sound Vib 293(1):156–170
22. Chowdhury I, Dasgupta SP (2003) Computation of Rayleigh damping coefficients for large systems. Electron J Geotech Eng 8.0
23. Altintas E (1995) Budak, analytical prediction of stability lobes in milling. CIRP Ann Manuf Technol 44(1):357–362
24. Özsahin O, Budak E, Özguven HN (2014) In-process tool point FRF identification under operational conditions using inverse stability solution. Int J Mach Tools Manuf
25. Gogu G (2008) Structural synthesis of parallel robots: part1—methodology, ISBN 978-1-4020-5102-9, Springer